Journal of Materials Chemistry A

Accepted Manuscript

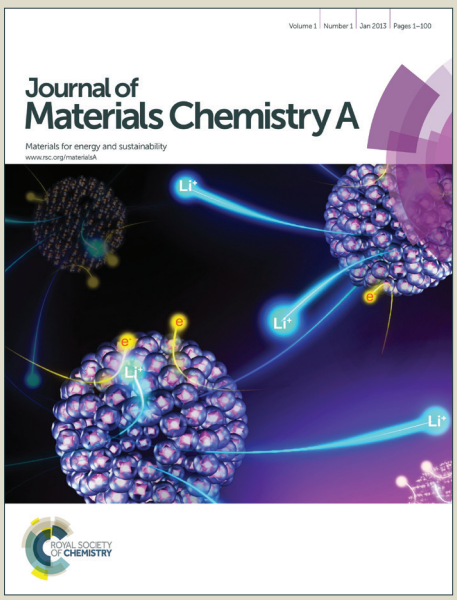

ROYAL SOCIETY OF CHEMISTRY

www.rsc.org/materialsA

Design of nitrogen doped graphene grafted TiO_2 hollow nanostructures with enhanced sodium store performances

Guohui Qin[*,a,b] , Xiaoyuan Zhang[a,b], Chengyang Wang[*,ab]

[a] *School of chemical Engineering & technology, Tianjin University, Tianjin 300072 , China.*

b Synergetic Innovation Center of Chemical Science and Engineering, Tianjin 300072,China.

Corresponding author:

Corresponding author.Tel./fax: +86 22 27890481.

E-mail address: guohuiq163@sina.com , cywang@tju.edu.cn.

Nitrogen doped graphene supported TiO_2 hollow nanostructures varied from 10-15nm were designed for sodium ion battery anode applications, which were obtained by a two step technique hydrothermal–calcining progress with urea as an inhibitor and nitrogen source.The active nitrogen modified graphene matrix supported hollow hierarchical–pore nanoarchitectures, possessing high surface area, massive pores including micro-,meso-and macro-pores, excellent structural stability, which are highly desirable for application in sodium ion batteries. Its interconnected carbon network ensures good conductivity and fast electron transport; the micro-,and meso-, and macroporous nature effectively shortens the sodium ion diffusion path and provides room necessary for volume expansion. The large specific surface area is beneficial for a better contact between electrode materials and electrolyte. Such material exhibits excellent performances as anode materials for sodium ion batteries with a high reversible capacity, excellent cycle stability and superior rate capability. Besides, nitrogen and graphene play a crucial role in controlling the formation of the TiO_2 hollow nanocrystals.

Introduction

Sodium ion batteries(SIBs) with Na ions as guest ions, are attractive in stationary

applications due to the cost and the availability advantage of Na over Li override their lower overall energy density.[1-3] However, considering of size of a sodium ion is obviously larger than that of a lithium ion, and thus there is a limited choice of electrode materials that are suitable hosts to accommodate Na ions and allow for reversible insertion–extraction reactions, which requires suitable host structures providing high storage capacity for facilitating its diffusion. In particular, there are very few reports of suggested anode structures for Na-ion batteries.[4-6]

Thus far, TiO_2-based composite with a high surface area have been identified as suitable Na-ion anode materials.[7-12] Nevertheless, TiO_2 have relatively low capacity to realize the high performance as anode materials.[13,14]The electrochemical performance of TiO_2 including the capacity ability is greatly affected by its morphology and structures. Careful control of the overall morphology of TiO_2 are highly desirable to obtain good rate performance and to gain reasonable capacities that make TiO_2 more competitive in sodium ion battery. Various kinds of nano/micro-structured TiO_2,such as nanoparticle, nanocrystal with controllable exposed facets (e.g.,{001}), nanorod, nanotube, hollow sphere/nanobox, and mesoporous and macro-/mesoporousTiO_2 have been successfully synthesized and investigated.[15-17]As a good electro-active material, it is expected that sodium ions would be able to electrochemically insert into TiO_2 hollow nanacrysals with the expected electrochemical performance.TiO_2 hollow composites are observed to ensure good electrode–electrolyte contact and serve as a fast diffusion pathway for electrolyte species in the cation intercalation process due to their high surface area and unique geometry. The porous structures are not only

conducive to lower current densities at the electrode–electrolyte interface, but are also beneficial for fully utilizing high electrochemical reaction rates per unit volume and enhancing diffusion kinetics, by reducing the diffusion pathway for electronic and ionic transport.[15,16]

Moving beyond simply considering the morphology of pristine TiO_2, tremendous efforts has been conducted on composite materials that contain TiO_2 and a secondary conductive phase. Pure TiO_2 suffers from intrinsic poor electronic conductivity ionic, and the limited specific capacity, which can be overcome by modifying structure and composition of pure TiO_2. Various conductive incorporations have been extended that exhibit a wide range of morphologies, which are often determined by the type of composites and production techniques.

Up to present, graphene sheets, atomic layers of graphitic carbons, are observed to present twice higher capacity of graphitic carbons, and exhibit some unique advantages such as excellent electrical conductivity, superior surface area, structural flexibility and chemical stability.[17-26] These features render graphene sheets to become an attractive and promising anode material candidate for lithium and sodium storage. Both theoretical and experimental studies have demonstrated that the intentional incorporation of heteroatoms (B, N, P and F) -doping into a graphene structure can significantly modify their adsorption energy, the diffusion and desorption barrier of lithium/sodium ions, in turn, resulting in the enhanced reversible capacity for lithium/sodium storage with respect to pristine graphene.[27-32]

Based on this pursuit, continuous efforts have been carried out to fabricate doped

graphene. Among them, N-doped graphenes (GN) are under intensive investigation to achieve high capacity and high rate capability, because GN can supply superior electrical conductivity facilitated for fast electron transport, high surface area, open and flexible porous structures available for numerous sodium storage sites, and short Li^+/Na^+ diffusion distances.[33-38]The introduce of GN to wrap TiO_2 crystallites in a conductive matrix allowing for the generation of different morphologies to facilitate titanium based composites with a designed structure for superior performance.[39,40]

In this work, the feasibility of electrochemical sodium storage in nitrogen doped hollow TiO_2 nanoparticles (G-TiO_2-N) with hierarchical pores is firstly evaluated for anodes in sodium ion batteries. As an anode material for SIBs, the hierarchical (G-TiO_2-N) nonacrystals exhibit high specific capacity, enhanced cycling stability, and good rate capability. More importantly, we employed a facile template-free synthesis route that may be scaled up for the target applications. In addition, the formation mechanism for the hollow nanoparticles was investigated by tracking the crystallization and morphology of the product at different reaction stages, which is proved to be the Ostwald ripening process.

Experimental section

Material Synthesis

Graphene oxide (GO) nanosheets was firstly synthesized from natural graphite powder by a modified Hummers method.[41]In a typical synthesis,30mLof ethanol/water (2:1,in volume) solution containing 6ml of titanium (IV) isopropoxide under air atmosphere via strong mechanical stirring at 10-80℃ were aged for 3h.The

precipitate was collected by centrifuge and repeatedly washed with ethanol and deionized water, and then air-dried at 80℃.In the following procedure,100mg of the as-prepared white powers and 20 mg urea ($CO(NH_2)_2$) were added into 10ml GO aqueous solution, subsequently, the mixture was sealed in a Teflonlined stainless steel autoclave with a pressure of 200 MPa and maintained at 180℃for 24 h;After washing with distilled water and ethanol several times, the collected composites were calcined at 700 ◦C for 10 h in a tubular furnace under a N_2 ambient to gain hierarchical hollow G-TiO_2-N composite. To prepare pristine TiO_2 and graphene doped TiO_2 (G-TiO_2) as comparison, the synthesis of G-TiO_2 was carried out in the absence of urea and the preparation of TiO_2were conducted without the addition of urea and GO under the same conditions and procedures as applied in the synthesis of composite. Scheme 1 illustrates the preparation process.

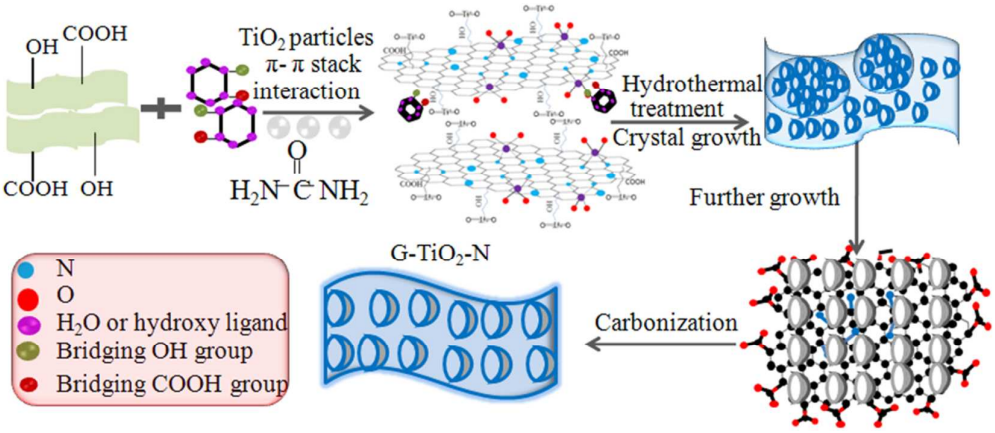

Scheme1 Schematic illustration of the synthesis procedure of G-TiO_2-N nanostructure.

Structural Characterizations

Powder X-ray diffraction (XRD) measurements were performed using an AXS D8 Advance diffractometer (Cu KR radiation; receiving slit, 0.2 mm; scintillation counter,40mA; 40kV) from Bruker Inc. The morphology and structure were obtained

on a JSM-7600F field emission scanning electron microscope (SEM),transmission electron microscopy (TEM) images by a Hitachi S-4800 field emission at an accelerating voltage of 200 kV and energy dispersive X-ray spectroscopy (EDX) of the samples Samples dropped on a carbon film supported on a Cu grid were obtained at 200 kV on a JEM-1200EX (Japan).Fourier transforms infrared (FT-IR) spectroscopy measurement was carried out with a NicoletNexus 5700 (Thermo Electron Corporation, USA) using KBr pellets. The nitrogen sorption isotherms (BET) were recorded by a Micromeritics ASAP-2020Mnitrogen adsorption apparatus. Pore size distribution plot was obtained by the Barrett Joyner Halenda (t-plot) method. The amount of carbon in the sample was determined by thermogravimetric analysis (TGA, NETZSCH STA 449 F3 apparatus) in air with a heating rate of 108C min^{-1}.The micro morphologies and the specific surface area.The compositions of samples were analyzed by X-ray Diffractometer (DX-2700,Haoyuan Corporation, China). X-ray photoelectron spectroscopy (XPS) data were obtained on an ESCALab220i-XL electron spectrometer (VG Scientific, West Sussex, U. K.) using 300 W Al Kα radiation. The base pressure was about 3×10^{-9} M bar.The binding energies were referenced to the C1s line at 284.5eV from adventitious carbon.

Electrochemical Tests

The evaluation of electrochemical performance was carried out by means of coin-type SIB cells (2025) assembled in an argon-filled glove box.For anode preparation, a mixture of active material, carbon black, and polyvinylidene fluoride (PVDF) binder with a weight ratio of 80:10:10 was dispersed in Nmethylpyrrolidone (NMP) solution,

and the resultant slurry was then uniformly pasted on a Cu foil current collector. A typical electrode was dried at 120 □for 24 h under vacuum before being assembled into coin cells in an argon-filled glove box. A Celgard 2400 microporous polypropylene membrane was used as the separator and sodium foil was used as the counter electrode. The nonaqueous electrolyte used was 1ml $NaClO_4$ dissolved in a mixture(1:1inwt%)of ethylenecarbonate(EC)/dimethylcarbonate(DMC).Galvanostatic cycling experiments of the cells were performed on a LAND CT2001A battery test system in the voltage range of 0.1–2.8V versus Na^+/Na at room temperature. The coin cells were activated at a current density of $50mAhg^{-1}$ for the first cycle, and then cycled under different current densities within the voltage range of 0.1-2.9 V using a LAND-CT2001A battery test system (Jinnuo Wuhan Corp.,China).Afterward, the cells were cycled under different current densities within the voltage range of 0.1-2.9 V. Electrochemical impedance spectroscopy (EIS) measurements were conducted on an electrochemical workstation (CHI 660 D,CHI Company) under a frequency range from 0.1 Hz to 100 kHz.

Results and discussion

The phase identification of the as-prepared TiO_2 was determined by X-ray diffraction (XRD) (Fig.1(a)).A series of diffraction patterns at 2θ = 25.8°, 38.3°,48.5.°, 53.9° and 55.5° corresponded to (101),(004), (200), (105) and (211) planes of TiO_2 according to the standardized JCPDS (21-1272) card.The effect of C and N on crystal was clarified by comparison of the XRD images, which shows that the diffraction peaks become broader with the addition of the carbon and nitrogen, implying the defects of the

nanocrystal introduced by carbon and nitrogen, which is further confirmed by the Roman spectroscopy. Also no diffraction peaks corresponding to C, N and other impurities were observed in these patterns. The (101) plane has the strongest line for all investigated TiO_2 samples. Using Scherrer's equation: $D=0.9\lambda/\beta\cos\theta$ where D is the average crystalline size, λ is the wavelength of Cu$K\alpha$ (λ=0.15406 nm), β is the full width at half maximum of the diffraction peaks, and θ is the Bragg's angle; the average particle size of TiO_2 was estimated to be around 100 (pureTiO_2), 25 (G-TiO_2), and 20 (G-TiO_2-N) nm, respectively. These datas indicated that the size of TiO_2 nanoparticle decreased with the modification of graphene, and further decreased with the incorporation of nitrogen, particle sizes of the as-prepared G-TiO_2-N was smaller than that of pure TiO_2.Presumably, the GN supported TiO_2 compounds limited further structural growth and the final size of TiO_2.It is noted that the ultrasmall hollow TiO_2 structures deliver short electron transport lengths which is unparalleled advantage compared to the other extended over micrometers in length structures.

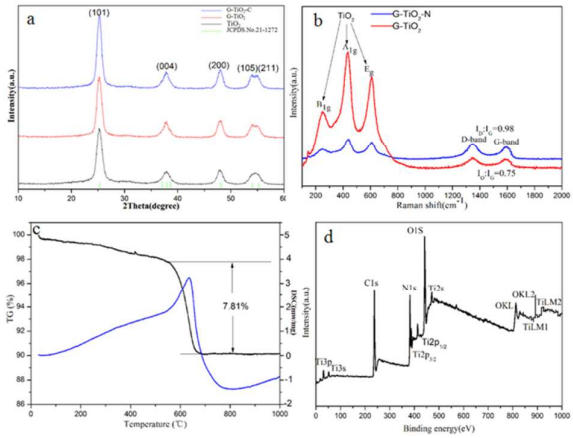

Fig 1.(a)XRD patterns of the TiO_2 samples;(b) Raman spectra of the TiO_2 composites;(c) TGA curves of the G-TiO_2-N composites under Oxygen flow;(d) XPS survey spectrum of G-TiO_2-N at 700 °C in NH_3 atmosphere for 1 h.

The pore size distributions of the as-prepared G-TiO_2-N calculated by desorption

isotherms using t-plot method are shown in Fig.S1.The Brunauer-Emmett−Teller (BET) surface area values calculated for the pure TiO_2, G-TiO_2 and G-TiO_2-N samples are respectively 49.2, 159.6 and 183.5g^{-1}.From DFT pore size calculations, the total pore volume values obtained for the three samples are respectively 0.04358, 0.05894 and 0.06013cm^3g^{-1}.The high specific BET surface area and the unique hollow characteristic provide a large G-TiO_2-N interfacial area, which is essential for the homogeneous distribution of hollow TiO_2 particles in the GN carbon matrix, and this result is confirmed by SEM images (Fig.3(c),(d)) and TEM images (Fig.4(d),(e)) of G-TiO_2-N. It can be found that the adsorption amount increases very sharply at low relative pressure (P/P_0), demonstrating the existence of micropores; and there exists a hysteresis loop after P/P_0=0.4 but without adsorption plateau near P/P_0=1.0,illustrating the presence of meso-and macropores. The G-TiO_2-N exhibits a distinct hysteresis loop in the range of 0.45−1.0 P/P_0, confirming the presence of a mesoporous structure with the maximum BET surface area. The surface area and abundant pores are of the necessities for a high electrochemical performance. The pore sizes distribution is found to centered around 15 nm (inset in Fig.S1).The identified porosity can be helpful in achieving the electrolyte solution and to accommodate the volume expansion of the TiO_2 nanoparticles when GN grafted hollow TiO_2 particles are used as an anode material for SIBs. Therefore, the as-prepared G-TiO_2-N has a unique three dimensionally interconnected hierarchical porous network. A scheme simulation of GN incorporated hollow TiO_2 particles is illustrated in Fig.2.

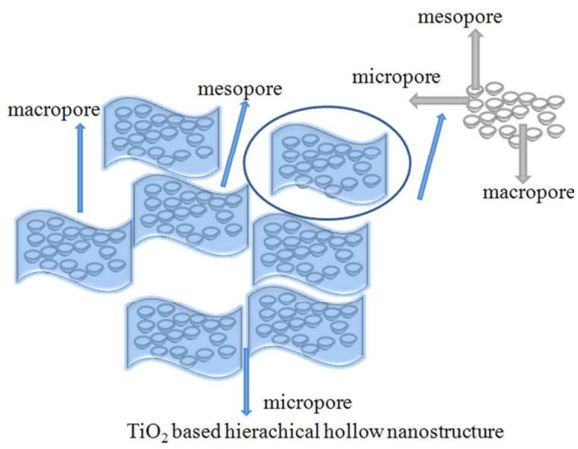

Fig.2 Scheme model of pore network of G-TiO_2-N.

Based upon these results, it is believed that the nanocrystals are expected to satisfy the demands of both fast ion transport and efficient ion-accessible surface area for charge storage.As to ion transport behavior, the nanostructures with the proper amount of three-dimensional interconnected meso-/macropores are sufficient to promote a global ion transport throughout the entire materials in the form of reducing the ion diffusion distance and transport resistance. As to ion adsorption behavior, the considerable number of micropores act as a crucial role in ion accumulation, which must be electrochemically accessible of ions.[42]

Raman spectra was carried out to investigate the crystalline phase of TiO_2 and the carbon type in the nanostructure (Fig.1(b)).Three peaks with strong intensities at 395, 515, and 635 cm^{-1} can be observed in the Raman files of the G-TiO_2-N nanocrystals, which are well consistent with that of reported anatase TiO_2.Two characteristic peaks located at about 1372-1592 cm^{-1} ascribed to disorder carbon (D-band) and graphite carbon (G-band) in the nanocomposite, respectively. The peak intensity ratio of D-band and G-band (I_D/I_G) is observed to be 0.98 for G-TiO_2-N compared to that of

the G-TiO_2 0.75 ,indicated that the existence of amorphous carbon and Nitrogen in G-TiO_2-N nanostructure. The total carbon content including graphene and nitrogen is directly obtained from the TGA.As can be seen from Fig.1(c), the weight loss of the precursor occurring in two steps corresponded with the peaks in the DSC curve. The first weight loss of 1.36% occurred between 100 to about 200℃, demonstrating the dehydration of surface-adsorbed water and graphene branched OH. The second weight loss of 7.81%,which was the major weightlessness step, occurred within the range of 200 to about 650℃ without further weight loss up to 1000℃ temperature, indicating the loss of CO_2, CO, NH_3 and H_2O.The corresponding endothermic peak was observed at 620.9℃ in the DSC curve. The weight loss was related to the decomposition of the graphene and nitrogen. In the TGA curve, there was an obvious plateau formed in the temperature range between 630 and 1000℃, which indicated that the stability of hollow TiO_2 particles.

The XPS result also evidenced the successful preparation of G-TiO_2-N, which provides an exact elemental composition in the top 0–12 nm depth of the sample surface(Fig.1(d)).The high resolution XPS spectra of GN (Fig.S2,) shows typical peaks at 284.72eV, 285.65eV, 287.46eV and 288.94eV from graphitic C=C/C–C, C=O and COOH bonds, respectively. In the spectrum of O1s the broad peak could be fitted into two symmetric peaks at 532.1 and 533.3eV,which arise from the graphene and the Ti–O bond, respectively (Fig.S3). The Ti_{2p} XPS spectra exhibits two characteristic peaks at 459.2 and 464.79eV, corresponding to the Ti $2p_{3/2}$ and Ti $_{2p1/2}$ spin–orbit peaks of TiO_2 (Fig.S4),suggesting that the valence state of Ti was still +4.

GN can be ascribed to a semiconductor with a good electro-conductivity. The binding energy shifts in the XPS spectra could be ascribed to the strong interaction (electron transfer) between the interweaved semiconductors because of their different Fermi energy levels.Considering the system finally reaches an equilibrium, when two or more nanoscaled semiconductors bind together, their Fermi energy levels have a tendency to adjust to the same value. Consequently, the electron concentration of the semiconductor with higher Fermi energy levels would decrease, correspondingly, decrease the electron screening effect and cause the enhancement of the binding energy.On the contrary, the electron concentration with lower Fermi energy levels would increase and hence will lead to the decrease of binding energy. Therefore, the higher binding energy shifts were related to the decreased electron concentration of TiO_2 hollow particles and increased electron concentration of GN nanosheets due to the electron transfer from pure TiO_2 nanostructures to GN nanosheets. It is suggested that the work function of the GN nanosheets may be larger than that of TiO_2 hollow particles.

SEM and TEM analyses were used to investigate the microstructure of the as-synthesized samples. As shown in Fig.3(a) and (b), the pristine TiO_2 composed of nanoparticles with an average diameter of about 100 nm have an obvious aggregation tendency, however, Fig.3(c) and (d) clearly reveals that the synthesized TiO_2 nanostructures with a much smaller size in the range of 10-15 nm are homogenously dispersed on the GN support with nearly no nanoparticles stacking, and GN thin films with little wrinkle and fold appear leaf like presenting a superior flexibility of the

whole nanosheet. Noticeably, the hollow feature of the TiO_2 nanocrystals are not obvious in the SEM image due to the ultrasmall size, but are certified in the following TEM results investigations.

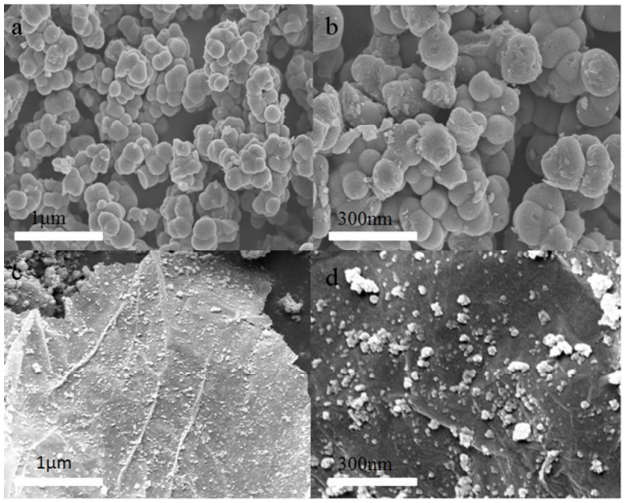

Fig.3 Images of (a) and (b) pure TiO_2 sample at various magnifications;(c)and (d) G-TiO_2-N composite at various magnifications.

Fig.4(a) and (b) showing the HR-TEM image of pure TiO_2 also presents aggregated particle-type structure with an average 100nm,which is in accordance with the SEM result. According to the TEM image of G-TiO_2-N composite shown in Fig.4 (d) ,(e)and(g), TiO_2 nanoparticles are well dispersed on the surface of Nitrogen doped graphene, indicating the uniform hybridization of GN with TiO_2 nanocrystals.

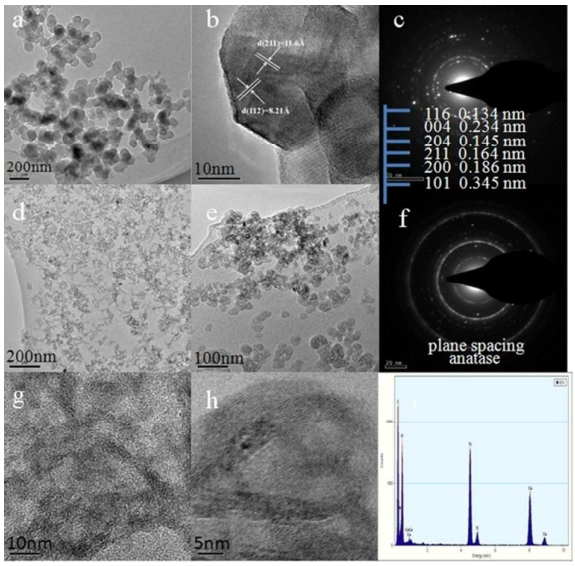

Fig.4(a)TEM image,(b)HRTEM image,(c)elected area electron diffraction (SAED) pattern for pristine TiO_2,(d) and (e)TEM image at different magnifications, (f) SAED pattern (g) and (h)HR-TEM image with different magnification, (i) element mapping for G-TiO_2-N.

Fig.4(d) (e), and (g) clearly indicate that theTiO_2 hollow nanoparticles were well dispersed and uniformly covered in the GN sheets which is consistent with the SEM image. The supported TiO_2 hollow nanostructures were reduced to 10-15nm from 100nm diameter nanoparticles, which is consistent with the FESEM analysis, XRD spectroscopy, and BET report. It is worthwhile to be pointed out, all hollow TiO_2 nanostructures are uniformly confined in the carbon matrix, further certifying that the unique hollow structure of the composite effectively endures the pulverization and prevents the particle aggregation, thus promises the long cycle stability.

Representative the high-resolution (HRTEM) images (Fig.4 (b)) displays that the TiO_2 particles were crystalline with clear lattice fringes parallel to the walls, the resolved lattice fringe with an interplanar distance of 0.81 and 1.16nm can be attributed to the (211) and (112) plane, respectively for plane of TiO_2 crystals. With an obvious contrast to the pure TiO_2, Fig.4(g) and (h) show mage of TiO_2

nanoparticles located on the surface of GN without clear interface, the resulting TiO_2 materials present a clear hollow nanostructure with ultra-thin walls. The ring pattern selected-area electron diffraction (SAED) in Fig.4(c) and (f) indicate the polycrystalline structure of the TiO_2 nanocrystals. The SAED pattern show reactions corresponding to the anatase TiO_2 phase. Some sharp reactions with values of 0.134, 0.234, 0.145, 0.164, 0.186, and 0.345 nm, represent diffraction from (116),(004), (204), (211), (200), and (101) planes of TiO_2 phase.Fig.4(i) depicts a typical EDS spectrum for the hybrids and Fig.5 reveals the corresponding elemental mapping of the hybrid samples, clearly showing that the synthesized hybrid products are composed of O, Ti, N and C elements with a homogeneous distribution for all the elements. It is also suggested the TiO_2 composite was uniformly dispersed along the GN surface, which showed highly developed hollow structures, as verified by the TEM images.

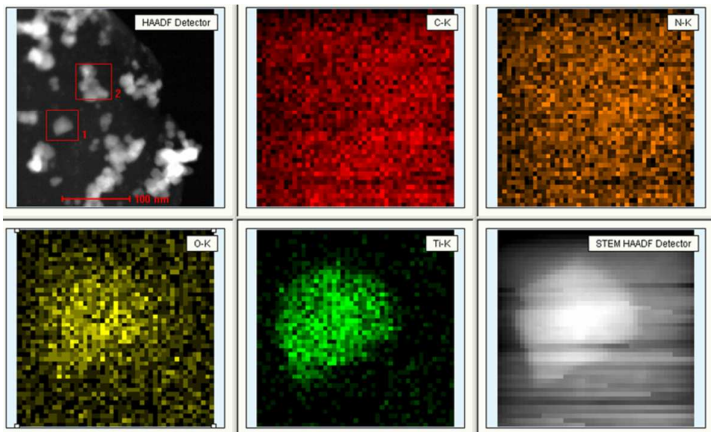

Fig.5HAADF-STEM image and corresponding EDS mapping images of an individual G-TiO_2-N indicating the homogeneous distribution of carbon, nitrogen, titanium, oxygen.

The growth mechanism of TiO_2 hollow nanostuctures is clarified by conducting a time-dependent change in the morphology of TiO_2.As shown by the TEM images in

Fig.6(a), after 6h of reaction under 180℃, nanoparticles with an average of 80nm are observed among the GN network, indicating the nanoparticles are gradually decreasing, hollowing and recrystallization, which is further verified by the following the evolution process. In each case the hydrothermally synthesized ripening mechanism occurred. In the first step, when TiO_2 particles with an average of 100 nm were added to the GO and urea solution, it formed a TiO_2 complex. After heating hydrothermally for 6h, the formation of densely packed particles of irregular shapes with dimensions of about 80 nm sizes were observed. These nanoparticles are composed of ultrafined particles which are loosely packed in the interior and tightly packed at the outer surface. When the reaction duration was increased further from 6h to 10 h, more and more particles at the interior get dissolved, and the diameter of the hollow core increases.The TEM image (Fig.S5) dedicates the hollow nanostructures with both inside and outside surrounded by the smaller particles homogenously distributed in the GN matrix. This results present the crystals are accompanied by the three variation program. When the heating duration was raised to 12h, the loosely packed bulk crystals (Fig.6 (b)) were continuously dissolved in the interior because of high energy and then recrystallized on the outer surface to yield ultrasmall hollow spheres(inset of Fig.6(b)) .

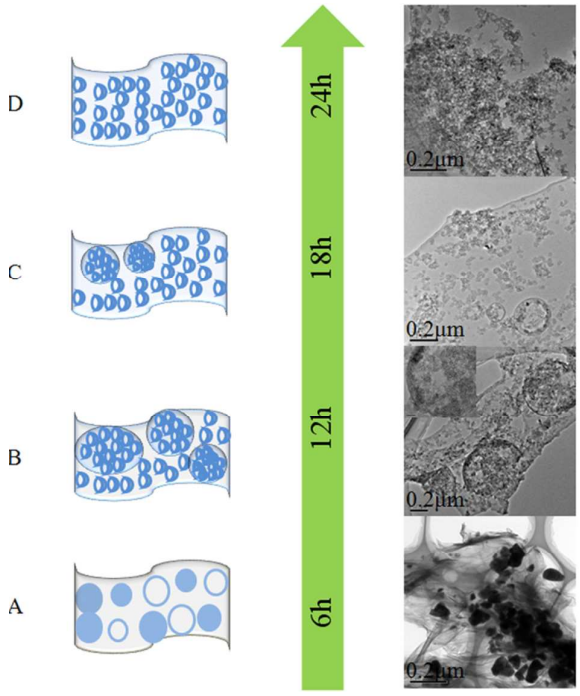

Fig.6 FESEM images of the peach-like hollow G-TiO_2-N at various time intervals: (A) 6 h, (B) 12 h, (C) 18 h and (D) 24 h.

Further increasing the reaction time to 18 h, the nanocrystals were further dissolved and ultrasmall hollow nanocrystals predominantly distributed in the GN support(Fig.6(c)). It is noted that the particle also follow the rule of growing and hollowing, evidenced by the TEM result (Fig.S6), most of small particles were hollow mixed up by some solid nanoparticles. Besides, HRTEM images (Fig.S6) reveals that the TiO_2 hollow nanoparticles locate on the surface of GN without clear interface, implying its strong incorporation with GN, which is beneficial to the electrochemical behaviors.

Finally, nanoparticle dissolution, hollowing, and recrystallization processes can complete in just 24 h under 180℃.Reactions with longer than 24 h produced hollow nanoparticles with the same shell thin thickness and interior space, well developed hollow nanostructures were uniformly distributed in the GN support with no obvious

aggregation due to the energy balance and the hollow characteristics tending to single distribution tendency. According to the phase field modeling,[43] the TiO_2 particle size reduces due to the complete wetting of surface facets, the nucleation barrier becomes smaller or even vanishing, consequently, the hollow ultrafined small nanocrystals were formed prone to nearly no aggregation, which can endure the volume variation during to the charge and discharge progress for sodium storage, which is highly desirable to observe a long life ability even at high current densities.

The roles of synthetic parameters like the effect of solvent, urea and key roles urea, solvent, and graphene for the formation of TiO_2 hollow spheres were analyzed systematically. The role of solvent (water) in steering TiO_2 nanostuctures growth was followed by using a different solvent, namely, ethanol.(100 mg of TiO_2, 24 h solvothermal treatment), the morphology of TiO_2 formed was different. The FE-SEM image (Fig.S7a) shows serious agglomerated shuttle-like particles. The roles of urea and graphene in the formation of TiO_2 hollow nanosturcture were determined by preparing TiO_2 with only graphene (no urea) and with sole urea (no graphene).The FE-SEM image of TiO_2 prepared from graphene shows (Fig.S7b) uniformly distributed nanoparticles, whereas the micrograph of TiO_2 obtained from the urea reveals (Fig.S 7c and d) the formation of densely packed particles of hollow nanostructures. In the case, the uniformity of the hollow structure does not obviously change, while the intensity of TiO_2 nanocrystals becomes increasingly aggregated. Clearly, these hollow nanocrystals form by a typical Ostwald ripening mechanism. Urea is a key precursor in this method, the urea plays dual roles in building the

anatase hollow nanostructures, which include:1) maintaining the uniform hollow structure and 2) reducing GO into graphene during the Ostwald ripening process, whereas water serves as a medium and graphene has an effect of minimizing agglomeration.Accordingly, these anatase hollow nanocrystals formed by inside-out Ostwald ripening.The channels for mass transfer during dissolving-recrystallizing process can finally result in rich porosity.

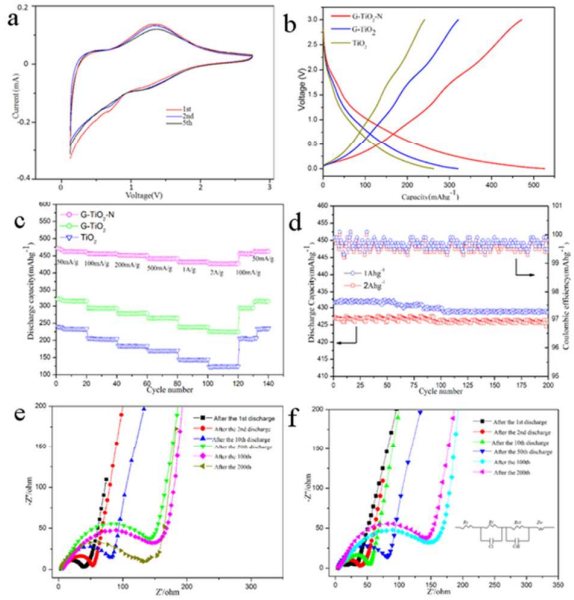

Fig.7(a) cyclic voltammogram curves with several cycles between 0.1V and 2.9 V (vs. Na^+/Na) at a scan rate of $1mVs^{-1}$; (b)Charge/discharge curves of TiO_2 samples at $50mAhg^{-1}$; (c) the cycle performances of the TiO_2 samples at various current rates;(d) long-term stability for G-TiO_2-N at a high current rate 1 A g^{-1} and 2A g^{-1};(e) EIS of G-TiO_2 electrode, the inset of (e) shows an equivalent circuit;(f) EIS of G-TiO_2-N electrode at different cycle numbers.

All the above investigations have demonstrated that the facilely obtained uniform hollow nanostructures possess pure anatase phase, high crystallinity, large surface area, and hierachical rich porosity. We could therefore expect these anatase hollow nanocomposite to exhibit enhanced electrochemical activity.

The electrochemical performance of the electrode was also evaluated by using a half-cell combined with a sodium metal electrode. Fig.7(a) shows the representative

cyclic voltammetry (CV) curves of the G-TiO_2-N electrode in a range of 0.1 to 2.9 V at a scan rate of 1 mV s^{-1}. As shown in Fig.7(a), the current beginning at 0.8V has related to irreversible formation of the solid electrolyte interface (SEI) in the first cathodic scan, in addition to the reversible sodiation of the material. By cycle 2nd a pair of redox peaks located at approximately 0.60 (cathodic) and 0.95 V (anodic) becomes appreciable and remains so with subsequent cycling. The 2nd and 5th cycles with higher cathodic peaks and lower anodic peaks compared with the initial cycle are nearly overlapped, indicating the high reversible electrochemical reactivity of G-TiO_2-N composites.

In Fig.7(b),the slope between 2.5 V and 0.5V has related to the insertion of sodium ions into GN grafted hollow TiO_2 nanostuctures and the reduction of Ti (IV) to Ti(III),followed by a long potential plateau, which is ascribed to the further sodium insertion. The slope below 0.5 V is associated with the formation of a solid electrolyte interface (SEI) film,[44-46]and the sodium storage on the surface or into the internal pores owing to their porous or hollow structures. The CV curve of the G-TiO_2-N has a combined shape of the GN and pure TiO_2, indicating that sodium ions are stored in both the TiO_2 and GN. The capacity of G-TiO_2-N (471.3 mAh g^{-1}) is about 1.47 times higher than that of G-TiO_2 (320.6 mA h g^{-1}) due to the active nitrogen introduce the pseudo capacity and the enhanced conductivity of GN, and is 2 times of that for pure TiO_2 (240.7 mA h g^{-1}) due to the hollow structure of the electrode material, which can not only effectively accommodate the volume expansion but also provide a mechanical support and perfect channels for the electrolyte penetration and Na^+

diffusion during the charging and discharging process. In addition, the protective GN layer is very important to maintain the stability of the structure, which could also improve the electronic conductivity and maintain the SEI Film on the surface.[47] In subsequent cycles, the pure TiO_2,G-TiO_2,and G-TiO_2-N show excellent capacity retention, which indicates the contribution of the hollow structure and interconnected GN layer to stabilizing the electrochemical activity of the anode materials.

The three types of electrodes were then subjected to cycling at various current densities from 50 mA g^{-1} to 2A g^{-1}.Fig.7(c) shows that the rate performance of the GN modified TiO_2 materials are substantially superior to that of pure TiO_2 and singly graphene modified TiO_2 composite. The profile of hollow TiO_2 combined with CN graphene present the best excellent cycling performance. Among these, the specific capacity of the G-TiO_2-N at a rate of 100 mAh g^{-1} is about 455.9 mAh g^{-1}, which is almost 1.55 times higher than that of TiO_2 nanoparticles combined with graphene (293.2 mA h g^{-1}) and is 2.23 times of that pure TiO_2 (203.9 mA h g^{-1}).As to G-TiO_2-N,the advantage of its rate performance is even more obvious, in other words, the gap between the discharge capacities of the G-TiO_2-N composite and bare TiO_2 and G-TiO_2 powders increased with increase in current densities, it still delivers a specific capacity as high as 426.8 mAh g^{-1}at the highest rate of 2A g^{-1},whereas the capacities obtained is just 224.3,124.3 mAh g^{-1},respectively, for G-TiO_2 and pureTiO_2.In particularly, the specific capacity of the TiO_2 based composites at 50 and 100 mAg^{-1} recover to their initial values due to its high reversibility. This exceptional cycle performance of G-TiO_2-N is caused by several synergistic functions, its hollow

structure can absorb the huge volume change during Na insertion and extraction reactions, the hierarchical pores offer an easy access to the sodium ions and the electrolyte during the cell operation, and graphene hinder the cracking or crumbling of the electrode, thus promoting the cycling stability. Furthermore, the higher conductive GN can improve the conductivity to enhance the rate performance.

The cycling behavior for the G-TiO_2-N electrode at a current density of 1 and $2Ag^{-1}$ is also shown in Fig.7(d).After 200 cycles, the discharge capacity of the G-TiO_2-N was still well retained with high capacities 425.6 mAh g^{-1}at a current density $2Ag^{-1}$after 200 cycles. The coulombic efficiency in the whole progress is beyond of 95%, indicating a good stability of the electrode of the GN grafted hollow TiO_2 nanostructures.The markedly improved electrochemical performance can be attributed to the hollow structure that can increase the surface areas, provide more active spots, shorten diffusion path lengths, accommodate the strain variations from sodium intercalation, and increase sodium storage capacity, and the unnegligible improved conductivity and ion diffusion facilitation supported by GN, which is consistent with the CV, charge-discharge and cycle performances.

In addition, in order to gain further insight into electrode microstructural changes during cycling, electrochemical impedance spectra (EIS) measurements were carried out in the frequency range of 10 M–0.01 Hz at 10 mV amplitude. The charge transfer resistance of the G-TiO_2 electrode after 10, 50 and 200 cycles increases from 52.5 to 77.8 and to 142.5, respectively (Fig.7(e)),however, this resistance is nearly unchanged for the following cycles with a value of 145.6 after 100 cycles. For the G-TiO_2-N

electrode, it increases from 50.2 (2^{nd} cycle) to 132.5 (100^{th} cycle),but stays comparatively stable in 138.9 (200^{th} cycle) after 100 cycles (Fig.7(f)),the consistently lower charge transfer resistance during cycling in G-TiO_2-N is accordance to the tendency in coulombic efficiency. This verifies that the GN matrix improve the ion accessibility and conductivity of the overall electrode. Furthermore, the hollow nanostructure channels facilitating each movement of Na ions while nitrogen doping gives a better conductivity than that of the pristine graphene without nitrogen-doping. In addition, to the possibility for our anode electrodes to be used as practical devices, the morphology variation of G-TiO_2-N before and after the 200 cycles were also investigated.

Fig.8 shows the textural variation of the G-TiO_2-N material after 200 charge/discharge cycles at $2Ag^{-1}$, compared with its TEM images (Fig.5(d)and (e)),the particle size and hollow structure, well distributed feature without obvious aggregation have been well kept and the structural integrity are still retained, indicating the robust structural stability of the material.Therefore, the EIS analysis agree well with the capacity/coulombic efficiency results, supporting that the electrodes are stable even after long cycling numbers at high current density. This confirms that the G-TiO_2–N nanocomposite could have so amazing cycling performance to make it attracting as the anode materials candidates for sodium-ion batteries.

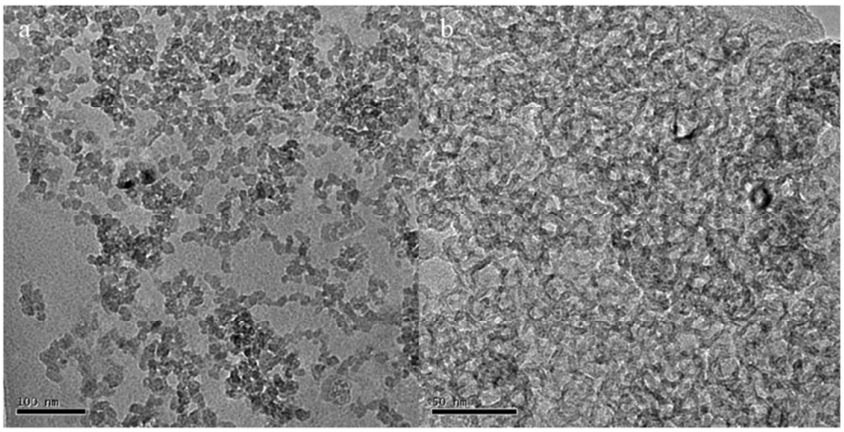

Fig.8(a) and(b) TEM images of G-TiO_2-N after 200th cycles at various magnifications.

Conclusions

In summary, the hollow TiO_2 nanocrystals were incorporated into interweaved framework of GN through a facile hydrothermal-calculation route.The precursor urea is vital during formation of the hollow TiO_2 nanostructure according to the Ostwald ripening mechanism investigation.The fabricated interconnected G-TiO_2-N material are based on the advantages of hierarchical hollow nanostructure and interconnected GN matrix, the hierachical hollow nanostructure are responsible for the facilitated transfer of sodium ions and the increased electron transfer. The exceptional cycle ability capability is benefitted from the unique thin wall hollow structure, which provides a significantly reduced path for both electron and ion diffusion, while the interconnected GN network has the intrinsically superior electrical conductivity for fast electron transport, high surface area, which is available for numerous sodium storage sites, and short Na^+ diffusion Distances. The electrochemical performance demonstrated that the developed G-TiO_2-N hybrids display considerably outstanding better capacity retention, excellent rate capability and high cycle stability compared to pure TiO_2

and G-TiO_2 materials. These results present the hollow hybrid is promising for high performance in SIBs applications.

Acknowledgements

The authors thankfully acknowledge the support of (No.51172160) for financial supports.

Notes and references

1 J. M.Tarascon, and M. Armand, *Nature* 2001, **414**, 359–367.
2 J. B.Goodenoughand, and Y. Kim, *Chem.Mater.*, 2009, **22**, 587–603.
3 D.A. Stevens, and J. R.Dahn, *J. Electrochem. Soc.*, 2000, **147**,1271–1273.
4 M.D.Slater, D. Kim, E.Lee, and C.S.Johnson, *Adv.Funct.Mater.*, 2013, **23**, 947–958.
5 V.Palomares, M.Casas-Cabanas, E.Castillo-Mart´ınez, M.H. Han, and T.Rojo, *Energy Environ. Sci.*,2013, **6**, 2312–2337.
6 H.A.Cha, ad- H. M. Jeong, and J. K.Kang, *J. Mater. Chem. A*, 2014, **2**,5182–5186.
7 S.Komaba , W. Murata, T.Ishikawa, N.Yabuuchi, T.Ozeki, T.Nakayama, A.Ogata, K.Gotoh,and K.Fujiwara, *Adv. Funct.Mater.*, 2011, **21**, 3859-3867.
8 X.Xia, and J. R.Dahn, *J. Electrochem. Soc.*, 2012, **159**, A515- A519.
9 J.F.Qian, X.Y.Wu, Y.L.Cao, X.P.Ai, and H.X.Yang, *Angew.Chem.,Int. Ed.*, 2013,**52**, 4633-4636.
10 A.Rudola , K.Saravanan, C.W.Mason ,and P.Balaya, *J. Mater.Chem. A*, 2013, **1**, 2653-2662.
11 W.Wang, C.J.Yu, Z.S.Lin, J.G.Hou, H.M.Zhu, and S.Q.Jiao, *Nanoscale*, 2013, **5**, 594-599.
12 H.G Wang, S.Yuan, D.L Ma, X.L Huang, F.L Meng and X.B Zhang, Adv. Energy Mater., 2013 DOI:10.1002/aenm.201301651. 9.
13 Z.H.Bi , M. P.Paranthaman, P.A.Menchhofer, R.R.Dehoff, C.A.Bridges , M.F.Chi, B. K.Guo, X.G.Sun, and S.Dai, *J.Power Sources*, 2013, **222**, 461-466.
14 Y.Xu, E.M.Lotfabad, H.L.Wang, B.Farbod, Z.W.Xu, A. Kohandehghan, and D.Mitlin,*Chem. Commun.*, 2013, **49**, 8973—8975.
15H.G.Wang,Z.Wu,F.L.Meng, D.L.Ma,D.L.Ma ,X.L.Huang,L.M.Wang,andX.B.Zhang,ChemSus Chem 2013, **6**, 56–60.
16 S.Yuan , X.L.Huang , D.L.Ma , H.G.Wang , F.Z.Meng, and X.B.Zhang, Adv. Mater. 2014, **26**, 2273–2279.
17 E.J.Yoo, J.Kim, E.Hosono, H.S.Zhou , T.Kudo, and I. Honma, *NanoLett.* 2008,**8**, 2277-2282.
18 S. B.Yang, X. L.Feng, and K. Müllen, *Adv. Mater.*, 2011,**23**, 3575-3579 .
19 S.B.Yang, X.L.Feng, L.Wang, K. Tang, J.Maier, and K.Müllen, *Angew.Chem. Int. Ed.*,2010 , **49** ,8408-8411 .
20 S.B.Yang, X.L.Feng, L.J. Zhi, Q.Cao, J.Maier, and K. Müllen, *Adv. Mater.*, 2010,**22**, 838-842 .
21Z.S.Wu, W.C.Ren, L.Xu, F.Li, and H.M.Cheng, *ACS Nano.*,2011 , **5**,5463-5471 .
22 G.X.Wang, X.P.Shen, and J.Yao, Park, J. *Carbon*, **2009** , *47* , 2049-2053 .
23 Hou, J. B. ; Shao, Y.Y.; M.W.Ellis, R. B.Moored, and B. L.Yi, *Phys. Chem.Chem. Phys.*, 2011 ,

13 , 15384-15402.
24Z.B.Lei, Y.Xiao, L.Q. Dang, W.S. You, G.S.Hu, and J.Zhang, *Chem. Mater.*,2007, **19**, 477-484 .
25 J.Li , E. B. Zhu, T.McLouth , C.Y.Chiu , X.Q.Huang, Y.Huang, *J.Am. Chem. Soc.*, 2012 , **134** , 12326-12329 .
26X.L.Huang, R.Z. Wang,D.Xu,Z.L.Wang,H.G.,Wang J.J. Xu ,Z.Wu,Q.C. Liu,Y.Zhang, and X.B. Zhang, 2013,**23**, 4345-4353.
27 A. L.M. Reddy, A.Srivastava, S. R.Gowda, H.Gullapalli, M.Dubey, and P.M.Ajayan, *ACS Nano*, 2010 , **4** , 6337-6342.
28 S.B.Yang, L.J.Zhi, K.Tang, X.L.Feng, J.Maier, and K.Müllen , *Adv.Funct.Mater.*,2012, **22** , 3634-3640.
29 X.Wang, X.Q.Cao, L.Bourgeois, H.Guan, S. Chen, Y.Zhong, D.M.Tang, H.Q.Li,L.Li, Y.Bando, and D. Golberg, *Adv. Funct. Mater.*,2012 ,**22** ,2682-2690.
30 H.B.Wang, C.J.Zhang, Z.H. Liu, L. Wang, P.X.Han, H.X.Xu, K.J.Zhang, S.M.Dong, J.H.Yao, and G. L.Cui, *J.Mater.Chem.*,2011 ,**21**,5430-5434.
31 C.C. Ma, X.H.Shao, and D.P. Cao, *J. Mater. Chem.*, 2012,**22**, 8911-8915.
32 L.Zhan, S.B.Yang, Y.Wang, Y.L.Wang, L.C.Ling, and X.L. Feng, *Adv.Mater. Interfaces*, 2014, 1300149.
33T.Q. Chen, Y.Liu, L.K.Pan, T.Lu, Y.F.Yao, S.Zhuo, Daniel, H.C.Chuab, and Q.Chen, *J. Mater. Chem. A*, 2014, **2**, 4117–4121.
34D.P.Nicholas,G.R.Stephen,E.W.Benjamin,M.Anwesha,andS.Andreas,*Inorg.Chem.*,2014,**53**,1100–1112.
35Y.G.Guo, Y.S. Hu, and J.Maier, *Chem.Commun.*, 2006, 2783-2785.
36 H.Zhang,G.R.Li,L.P.An,T.Y.Yan, X.P.Gao, and H.Y.Zhu, *J.Phys.Chem.C*, 2007,**111**, 6143-6148.
37S.Brutti, V.Gentili, H.Menard, B.Scrosati, and P.G.Bruce, *Adv. Energy Mater.*,2012,**2**, 322-327.
38S.Liu, J. J.Hu, N. F.Yan, G.L.Pan, G. R.Li, and X.P.Gao,*Energy Environ. Sci.*,2012,**5**, 9743-9746.
39 R.Liu, Y.Ren,Y.Shi,F.Zhang, L.Zhang, B.Tu,and D.Zhao, *Chem. Mater.* **2008**, 20, 1140−1146.
40J.S.Chen, Z.Wang, X.C.Dong, P. Chen, and X.W. Lou, *Nanoscale*, 2011, 3, 2158−2161.
41D.C.Marcano, D.V. Kosynkin, J.M.Berlin, A.Sinitskii , Z.Z.Sun , A. Slesarev , L. B. Alemany , W. Lu and J. M. Tour, ACS Nano,2010,**4**:4806-4814.
42F.Xu,;R.J.Cai,Q.C.Zeng,C.Zou,D.C.Wu,F.Li,X.Lu,Y.Liang, and R.Fu, *J.Mater.Chem.*,2011, **21**, 1970–1976.
43 D.A.Cogswell, and M.Z.Bazant, *Nano Letters*, 2013**,** **13**, 3036-3041.
44X.Yan,;Y.J.Li,F.Du,K.Zhu,Y.Q.Zhang,A.Su,G.Chen,andY.J.Wei,*Nanoscale*,2014,**6**, 4108–4116.
45 Z.M.Cui, L.Y.Jiang, W.G.Song, and Y.G. Guo,*Chem.Mater.*,2009,**21**, 1162–1166.
46Y.Z.Su, S. Li, D. Q.Wu, F.Zhang, H.W.Liang, P. F.Gao, C.Cheng, and X.L.Feng, *ACS Nano*, 2012, **6**, 8349–8356.
47A.S.Aric,P.Bruce, B.Scrosati, J.M.Tarascon, and W.V.Schalkwijk,*Nat.Mater.*2005, **4**, 366–377.

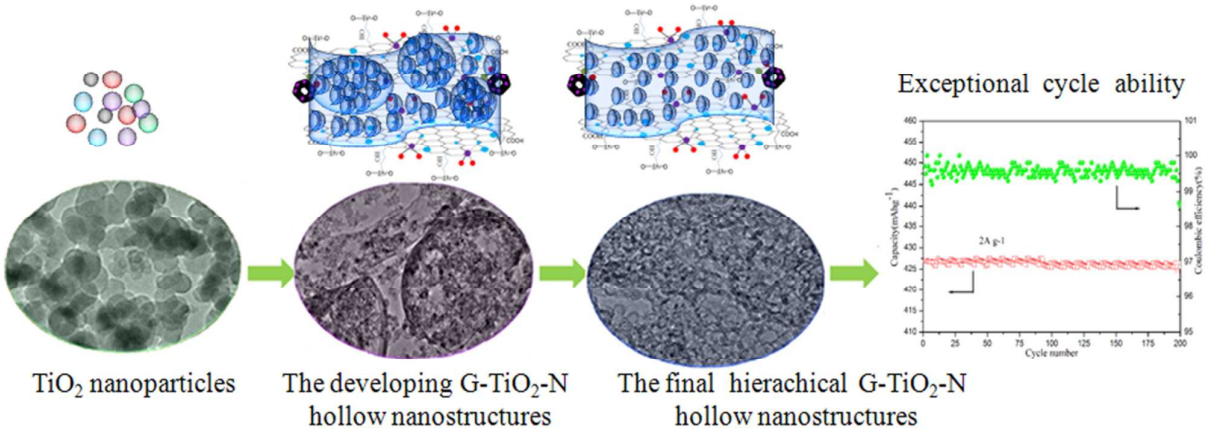

A N-doped graphene grafted hollow TiO_2 nanostructures were fabricated and evaluated as a promising candidate for sodium store